



Lunar regolith thermal behavior revealed by Chang'E-1 microwave brightness temperature data

Kwing L. Chan^a, Kang T. Tsang^{a,*}, Bruce Kong^a, Yong-Chun Zheng^b

^a Center for Space Science Research, Hong Kong University of Science and Technology, Hong Kong, China

^b National Astronomical Observatories, Chinese Academy of Sciences, Beijing 100012, China

ARTICLE INFO

Article history:

Received 7 September 2009

Received in revised form 2 April 2010

Accepted 8 April 2010

Available online 10 May 2010

Editor: T. Spohn

Keywords:

Moon

microwave

brightness temperature

Chang'E-1

data

map

ABSTRACT

Microwave brightness temperature data obtained by the Chinese Chang'E-1 lunar orbiter are analyzed with the lunar diurnal variations filtered. Resulting maps from the high frequency microwave channel show lunar topographic signatures with close similarity to those seen in Clementine's lunar topography maps, while the low frequency channels reveal intriguing lunar surface properties not previously observed. Here we focus on two characteristics displayed by the filtered brightness temperature maps: in the high frequency maps the existence of an anti-correlation between daytime and nighttime brightness temperature deviations in certain regions (especially in the lunar maria), and in the low frequency maps the appearance of cold spots which correspond with the hot spots observed in the infrared during lunar eclipses.

© 2010 Elsevier B.V. All rights reserved.

1. Introduction

Chang'E-1 (CE-1), the first Chinese lunar orbiter, was launched on October 24, 2007 and operated until March 1, 2009 when it crashed onto the surface of the Moon in a controlled impact. During CE-1's life time of more than a year, it covered the entire surface of the Moon many times in a precessing polar orbit 200 km above the lunar surface, transmitting 1.38 terabytes of data to Earth. In this letter, we describe the initial results from our analysis of the data obtained by CE-1's Lunar Microwave Radiometer (MRM).

Ground-based microwave brightness distribution maps of the nearside of the Moon had been obtained since the pre-Apollo era (e.g. Coates, 1961; Gary, 1967; Moffat, 1972; Schloerb et al., 1976). Compared to infrared radiation, microwaves originate from deeper layers and contain information about the physical properties of the regolith below the surface. Radar studies can probe deep and produce high-resolution maps (e.g. Zisk et al., 1974; Margot et al., 2000; Campbell et al., 2007), but do not provide information about the thermal behavior of the regolith. From space, lunar brightness temperature data were derived (Lawson et al., 2000) from images acquired by the Clementine's Long Wavelength Infrared camera (Nozette et al., 1994). Recent lunar orbiters, KAGUYA (Ono et al., 2009) and Chandrayaan-1 (Goswami and Annadurai, 2008), have

obtained active radar images of the Moon. CE-1's microwave radiometry dataset is the first obtained from a passive sensor in lunar orbit, and covers the entire Moon in unprecedented spatial resolution and temporal span. Here, we show that when the diurnal variations of the brightness temperatures (TB) are filtered from the data, the resultant maps demonstrate detailed correspondence with lunar geographic features.

The DIVINER experiment on board Lunar Reconnaissance Orbiter is making high-resolution and global observation of the Moon in the spectral range 0.3–200 μm . Its year-long mission will provide important data about the surface temperature distribution and variation over most of the lunar diurnal cycle. The information can provide surface boundary conditions for further interpretation of CE-1's microwave data set.

The microwave thermal emission from the lunar surface layer is affected by a number of physical parameters including the dielectric constant, loss tangent, thermal conductivity, density, heat flow, and heat capacity (Krotikov and Troitsky, 1964; Keihm and Langseth, 1975a; Schloerb, et al., 1976; Naugol'naya and Soboleva, 2001). These physical parameters are in turn related to constituents of the regolith including metal abundances (especially that of titanium) and rocks of different sizes (Fisher and Staelin, 1977; Mendell and Wicczorek, 1993). CE-1's microwave data will be important for constraining the ranges of the physical parameters and for studying the physical/chemical environment of the lunar surface layer. This represents a large number of applications. The aim of the present letter is only to

* Corresponding author. United International College, Zhuhai, China.

E-mail addresses: maklchan@ust.hk (K.L. Chan), k2tsang@gmail.com (K.T. Tsang).

present a preliminary overview of the MRM data and to highlight some interesting observations.

2. Methodology

The MRM is one of the scientific payloads onboard CE-1, operating in four microwave frequency channels: 3, 7.8, 19.35 and 37 GHz (to be labeled as channels 1–4, with wavelengths 10, 3.84, 1.55, and 0.81 cm, respectively). All four channels are estimated to have a sensitivity of 0.5 K in brightness temperature. The spatial resolutions on the lunar surface are in the range 35–50 km (best for the highest frequency channel). The real-time calibration used two reference sources. The hot reference was an internal source of 300 K, and the cool reference was the 2.7 K space background. The space background however could be affected by astronomical bodies (e.g. the Sun, Earth, and bright stellar systems). During such incidence, the calibration was temporarily frozen. Detail description of the instrument and its characteristics can be found in Wang et al. (2009). The regolith depths into which the MRM channels can sense depend on the constituents of the regolith layer. In general it is expected that such depth is no more than a few centimeters for the 37 GHz waves and 10 m for the 3 GHz waves (Keihm and Langseth, 1975b; Fa and Jin, 2007).

Raw data received from MRM are preprocessed by Chinese Academy of Sciences to a distributable PDS (Planetary Data System) format. In the final form employed in this analysis, the relevant quantities in each record are: the UTC time of the measurement, brightness temperatures from the four microwave channels, solar incidence angle, solar azimuth angle, the orbital information of CE-1 (longitude, latitude, and orbital altitude), and data quality state. Besides using the data quality state indicator, the obviously bad data are removed by restricting all TB values to the range 20–500 K (about 0.04% of the entries were eliminated).

Unlike surface temperature on the Earth (which depends on the atmospheric conditions), local surface temperature on the Moon depends primarily on its spatial relationship with respect to the Sun. Signals in TB that reflect the local properties of the regolith can be easily masked by the diurnal (day/night) variation. To extract the regolith signals, it would be useful to subtract the diurnal variation from the TB, if a model for the variation can be constructed. Under the fortunate circumstance that the equatorial plane of the Moon is within 1.6° from the ecliptic plane, it is a good approximation to consider the diurnal variation of solar influence a function of the hour angle and the lunar latitude only (for locations not too close to the poles). Hence the first step in our analysis is to establish the dependence of TB on the hour angle and the lunar latitude.

Instead of making assumptions on the diurnal dependence based on observations in short wavelengths (Pettit and Nicholson, 1930), we employ numerical model fits that minimize the root-mean-square (rms) deviations, by expansion in spherical harmonics to 4th degree. In Fig. 1, a comparison of the model fits and data at the latitudes 0°, 40°, and 60° North (within bands of 0.1° half-width), for the highest frequency channel (37 GHz) is shown. The vertical axis is the brightness temperature in degree K, the horizontal axis stands for the hour angle (−180° to 180°) starting with midnight on the left. The periodic variation along the hour angle direction represents the diurnal effect and peaks near the equator. The maximum value of the model is 288 K, and it lags behind noon for about 33°. Similar models are obtained for the other frequency channels. The rms deviations of the TB data from the model fits are 2.2, 3.6, 3.3, and 3.6 K for channels 1–4, respectively. These deviations, which include surface roughness and microwave emissivity variations, are quite small compared to the full range of temperature variations (except for the lowest frequency). Included is also a ‘seasonal’ effect caused by the change of distance between the Earth and the Sun during the data accumulation period. This effect is responsible for creating a substantial fraction of the data’s rms deviation from a diurnal model (2–2.5 K). The fact that the

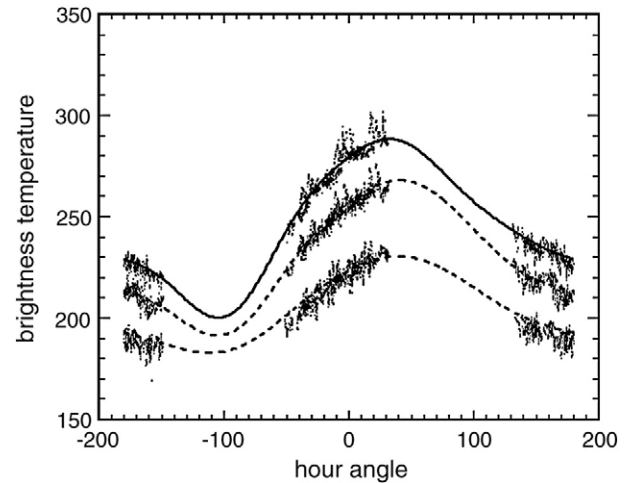


Fig. 1. Diurnal and latitudinal variation model for data from the 37 GHz frequency channel. The vertical axis shows the brightness temperature in degree K. The horizontal axis shows the hour angle with noon denoted by 0°, and midnight by 180° (or −180°). Ordered from top to bottom, the three curves represent model values at the latitudes 0°, 40°, and 60° N. The scattered points show TB values observed within latitudinal bands $\pm 0.1^\circ$ from these three latitude values.

maps can clearly display known topographical features (see later discussion) also argues for significantly smaller instrumental errors achieved by CE-1 MRM.

Our diurnal variation models give us the ability to map the brightness temperature of the Moon in a more informative way. We filter out the diurnal variation and ‘normalize’ the temperature deviation by forming the scaled temperature deviation $\tau = (TB - TB_{\text{model}}) (TB_{\text{ref}}/TB_{\text{model}})$ where TB_{model} is the model TB and TB_{ref} is a reference temperature. TB_{ref} is taken to be the equatorial noon time (midnight) model temperature for daytime (nighttime) data. The values of TB_{ref} for the different channels are given in Table 1. The scaling factor ($TB_{\text{ref}}/TB_{\text{model}}$) is introduced to offset the effect of non-vertical solar incidence (to simulate a uniform sub-solar (daytime)/anti-solar (nighttime) condition) so that the contrasts produced by surface features are accentuated. Different powers of this ratio have been tested, and the present choice gives the best map contrast. This process distinguishes the maps here from the previous ones (e.g. Zheng et al., 2009). The τ maps reveal features that depend on combined effect of local topography and soil physics. While maps constructed from the highest frequency data reveal mainly the surface, low frequency maps contain information of deeper layers.

3. Results

Examples of our results are shown in Figs. 2 (37 GHz) and 3 (3 GHz), in which daytime (upper panel) and nighttime (lower panel) maps of the scaled temperature deviation (τ) from two of the microwave channels (the highest and the lowest frequencies) are shown. To avoid the masking effect of the deep topographic shadows in the polar regions (which also causes the deterioration of accuracy in the fitting of diurnal variations), we truncate the map at 60° latitude north and south. The data are collected and averaged in

Table 1
TB of the diurnal models at the equator.

Channel	Noon temperature	Midnight temperature
1	226.7	224.0
2	251.2	243.5
3	261.7	236.3
4	279.5	228.9

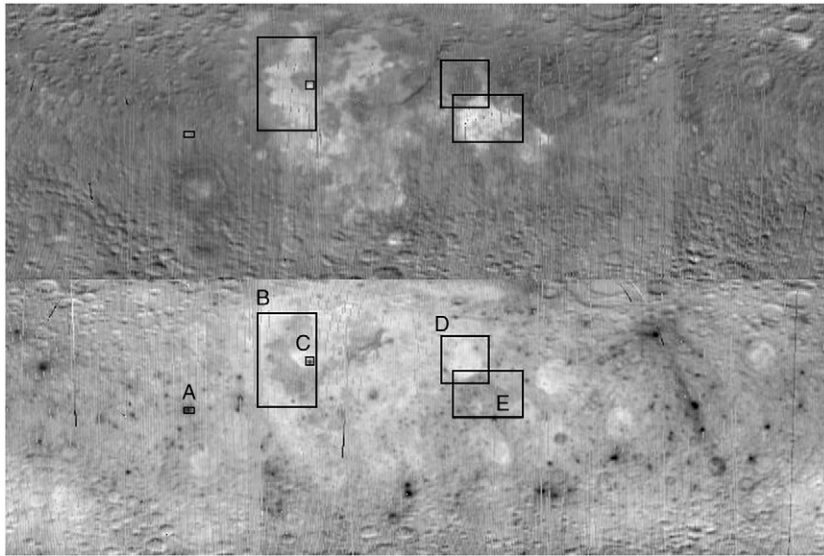


Fig. 2. Daytime (upper panel) and nighttime (lower panel) τ maps of the 37 GHz channel, for the lunar region with $-60^\circ < \text{latitude} < 60^\circ$ and $-180^\circ < \text{longitude} < 180^\circ$. Bright/dark colors show high/low values; in the daytime panel the maximum and minimum values of τ covered by the grey scale range are 18 K and -19 K, respectively, while in the nighttime panel they are 8 K and -20 K. The rectangular boxes enclose prototypical features of special interest (see text).

$0.5^\circ \times 0.5^\circ$ bins (averaged number of data entries per bin ~ 19). Each map shows 720×240 uniformly distributed bins (simple cylindrical projection). The longitude and latitude ranges are $(-180^\circ$ and $180^\circ)$ and $(-60^\circ$ and $60^\circ)$, respectively. Due to the oblique illumination which produces shadows in a landscape with varying slopes, the topographic features are clearly exhibited in the top panel of Fig. 2 which represents the daytime TB data from the highest frequency channel and best reflects the surface condition.

3.1. Day/night correlation

In the highest frequency channel, most of the large maria show temperature excess of about 10 K. This is close to earlier results in shorter wavelengths (Gary, 1967; Lawson et al., 2000). An interesting behavior of mare TB in this frequency is the anti-correlation of day/night deviations. The correlation coefficients of daytime and night-

time scaled brightness temperature deviations (τ) within the rectangles A–E marked on Fig. 2 are listed in Table 2 (deviations are relative to the regional mean values; bad data strips have been eliminated). The second column of the table shows the ranges of longitude and latitude covered by the rectangles. Columns 3 to 6 show the correlation coefficients given by the four microwave channels. The rectangles B, D, and E roughly enclose the upper part of Oceanus Procellarum, Mare Serenitatis, and Mare Tranquillitatis. In the highest frequency, the correlation coefficients for these mare regions are evidently negative. Note that compared to its surroundings, the daytime τ of Mare Serenitatis is slightly depressed (about -3 K), while its nighttime τ is elevated (about $+5$ K). Therefore, not all maria have daytime TB excess. Furthermore, day/night anti-correlation of τ in the maria is not universal. Mare Crisium (not enclosed by the rectangles) indicates a mild positive correlation (~ 0.3). In the lowest frequency channel (channel 1), most maria still show elevated

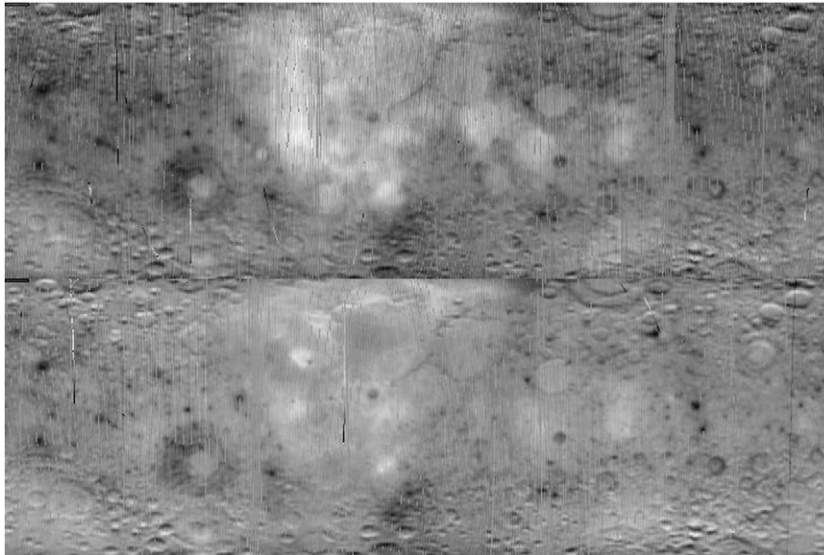


Fig. 3. Daytime (upper panel) and nighttime (lower panel) τ maps of the 3 GHz channel, for lunar region with $-60^\circ < \text{latitude} < 60^\circ$ and $-180^\circ < \text{longitude} < 180^\circ$. Bright/dark colors show high/low values; in the daytime panel the maximum and minimum values of τ covered by the grey scale range are 9 K and -10 K, respectively, while in the nighttime panel they are 7 K and -10 K.

Table 2
Correlation coefficients of day/night τ in the rectangular regions of Fig. 2.

Label	Extent	Channel 4	Channel 3	Channel 2	Channel 1
A	(−102, −98) × (2, 4)	−0.62	+0.27	+0.81	+0.94
B	(−70, −45) × (5, 45)	−0.83	−0.71	−0.25	+0.29
C	(−49, −46) × (23, 26)	−0.90	−0.76	−0.18	−0.21
D	(10, 30) × (15, 35)	−0.84	−0.71	−0.28	−0.07
E	(15, 45) × (0, 20)	−0.66	−0.62	−0.07	+0.16

TB deviations during day time ($\tau \sim 4$ K). The day–night anti-correlation of τ , however, vanishes. This is shown in the last column of Table 2.

Day/night anti-correlation is not limited to mare regions, certain craters also show such behavior, as is demonstrated in the rectangles A (an unnamed highland crater near Lenz Crater; Mendell and Wieczorek, 1993) and C (the bright Aristarchus Crater) of Fig. 2. The channel 4 correlation coefficients in these two regions are negative.

The anti-correlation between daytime and nighttime τ in the high frequency channels reflects thermal properties of the upper regolith of the feature. It may be explained as the surface material heating up to a relatively higher temperature than average during the day and cooling down to a relatively lower value at night. In the channels with successively lower frequencies, the anti-correlation gradually diminishes (see Table 2). This is compatible with the interpretation that the longest wavelength microwave can penetrate deep into the thermal absorption layer. The daytime τ map of channel 4 shows striking similarity to the titanium distribution map derived from Clementine's ultraviolet–visible data (Lucey et al., 1996; Gillis et al., 2003; <http://www.lpi.usra.edu/lunar/missions/clementine/images/>). It is suggestive of a close connection.

Besides the maria, the display of rings (e.g. Humboldtianum, and Moscoviense) and rays (e.g. Orientale) around some large craters is also noteworthy. The long ejecta streak that runs between Giodano Bruno Crater and Necho Crater is striking, but is only prominent in the nighttime maps of the channels 3 (not shown here) and 4. The bright and dark faces of crater rims in the high latitude regions are characterized by positive correlations across all maps (different channels, day and night).

3.2. Nighttime cold spots

The most interesting features revealed by the τ maps are the conspicuous nighttime cold spots (and patches), especially evident on the highlands. These are small regions less than a few degrees in diameter (some may be below resolution limit), and are a few percent cooler than their surroundings (about 3% in channel 1 and 6% in channel 4). They consistently appear on nighttime maps of all frequency channels (e.g. lower panels of Figs. 2 and 3), and also on the daytime maps of the low frequency channels (e.g. upper panel of Fig. 3). In the high frequency daytime maps (e.g. upper panel of Fig. 2), some of them appear as 'hot spots' (e.g. at Aristarchus, Giodano Bruno, King, and Necho where τ reaches 20, 17, 7, and 7 K, respectively), but more generally, the high daytime temperature often masks their presence. The day/night correlation coefficients of a rectangle barely covering a cold spot (or patch) generally take on values similar to those of region A listed in Table 2. The anti-correlation in the highest frequency channel is negative but mild. In the lowest frequency channel, the correlation turns positive and the value is high (region C, Aristarchus, is exceptional).

It turns out that these nighttime cold spots correspond closely with the 'hot spots' found in the infrared (10–12 μm) during lunar eclipses (e.g. Shorthill and Saari, 1965). With rare exceptions, the 'cold spots' can be identified by 'hot spots' shown in the infrared atlas charts of Shorthill (1973), as long as the region is covered by the charts. The number (~ 200) and density of CE-1 'cold spots' are much less than the number and density of 'hot spots' shown in the Shorthill charts. This may be due to the lower spatial resolution of the

microwave channels and/or lower signals coming from beneath the surface. If the nighttime 'cold spots' in microwave are truly related to the 'hot spots' in infrared during eclipses, new constraints can be put on the spots' thermal properties.

3.3. High latitude regions

In the polar regions, the deep shadows created by topography make the detection of nighttime 'cold spots' difficult. Beyond 70° north or south, the variations induced by the shadows are so intense and strong that non-topographical features with a few percent variations cannot be recognized. Polar topographical shadows harbor their own cold patches which are of interest to the search of water ice (Feldman et al., 2000). Fig. 4 shows a composite of four maps. North and South poles are shown on the left and right, respectively. The upper panels show unfiltered channel 4 TB and the lower ones show unfiltered channel 1 TB. The boundaries of the disks are at the 80° latitude circles. The brightness temperatures are collected in 3×3 km² bins and averaged over the whole data period (day and night). Therefore, the dark areas are truly cold, in both day and night. In the north, only one location at Peary Crater (88.6° N, 33.0° E) is truly dark, which means that the local temperature minima are independent of day and night (relative minima of TB in channels 1 and 4 are 58 and 70 K, respectively). In the south, the pole-ward region of Malapert Mountains shows the deepest dips in temperatures (52 and 65 K in channels 1 and 4, respectively). The cold patch at Cabeus Crater (84.9° S, 35.5° W), which has recently been studied by a rocket impact from the LCROSS mission, also shows day/night independence, but the temperature dips (65 and 72 K in channels 1 and 4) are not as deep as the other. Note, however, that these local minima are obtained after averages over bin areas and time have been made; they are not the minimum values obtained by the MRM instrument at a single instance and location.

Cold patches in the polar regions are different from those revealed by CE-1 data in mid- and low-latitudes. Due to the low elevation of the

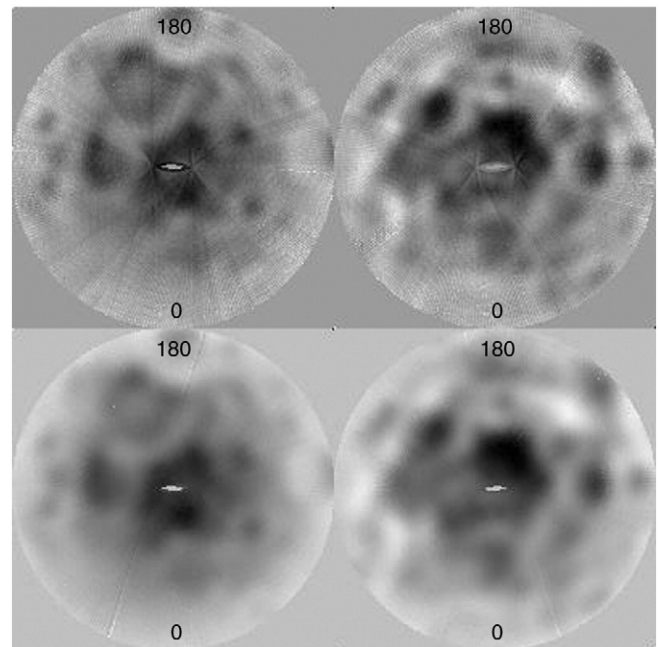


Fig. 4. 'Temporally averaged' TB maps showing cold areas near the poles. North and South Pole regions are shown on the left and right, respectively. The upper/lower panels show unfiltered channel 4/channel 1 brightness temperature accumulated and averaged over both day and night. The boundaries of the disks are at the 80° latitude circles. The maps use satellite projection from large distance. The 200×200 bins are squares with equal area on the projected plane. In the upper panels the grey scale spans the range 64 K to 180 K; in the lower panels it spans the range 50 K to 130 K.

Sun in the polar regions, the rims of craters cast very long shadows and areas inside certain craters are never exposed to sunlight. The temperatures in the interiors of such craters thus remain very low day and night. This type of cold patches is not due to specific physical property associated with the regolith. In contrast, the ‘cold spots’ in mid- and low-latitudes discussed earlier cannot be explained simply as consequences of oblique illumination or shadows of steep landscapes. They are most likely related to distinct physical/thermal properties of the surface layer of the Moon.

4. Conclusions

CE-1’s microwave τ map results are primarily compatible with earlier observational results obtained in other electromagnetic wave bands. The maria show their prominent presence with generally higher TB. Topographic features are displayed through the variation of illumination. However there are also significant new results. The maria TB do not strictly follow the albedo distribution. The microwaves can probe deep into the Moon’s thermal absorption layer and tell more about the physical properties of the surface layer of the Moon. The role of titanium in affecting the thermal properties of the lunar surface is clearly reflected. The infrared hot spots observed during lunar eclipses apparently turn into microwave cold spots after long cooling time. Assessing theories for the spots (e.g. Roelof, 1968; Winter, 1970) is beyond the scope of the present letter, but CE-1’s microwave data will certainly play a role in this pursuit.

The CE-1 MRM has produced valuable data for studying a number of important problems associated with the lunar regolith (e.g. Keihm and Langseth, 1975a; Jin and Fa, 2009). The information on diurnal variations of the multi-channel TB at various sites will prove to be crucial in constraining the thermal/radiation properties and the modeling of the lunar surface materials.

Acknowledgements

We would like to express our gratitude to Dr. Bruce Campbell and an anonymous referee for their valuable comments and suggestions which have led to major improvement of the manuscript, including the discovery of association between the microwave cold spots and the infrared hot spots found during lunar eclipses. We thank the National Astronomical Observatories of Chinese Academy of Sciences for the technical assistance. This work is supported by the Research Competitive Program, School of Science of the Hong Kong University of Science and Technology, the Research Grants Council of Hong Kong, and was partially supported by a grant from the National High Technology Research and Development Program of China (863 Program) and the National Natural Science Foundation of China (no. 40904051).

References

Campbell, B.A., Campbell, D.B., Margot, J.L., Ghent, R.R., Nolan, M., Chandler, J., Carter, L.M., Stacy, M.J.S., 2007. Focused 70 cm wavelength radar mapping of the Moon. *IEEE Trans. Geosci. Remote Sens.* 45, 4032–4042.

Coates, R.J., 1961. Lunar brightness variations with phase at 4.3-mm wave length. *Astrophys. J.* 133, 723–725.

Fa, W., Jin, Y.-Q., 2007. Quantitative estimation of helium-3 spatial distribution in the lunar regolith layer. *Icarus* 190, 15–23.

Feldman, W.C., Lawrence, D.J., Elphic, R.C., Barraclough, B.L., Maurice, S., Genety, I., Binder, A.B., 2000. Polar hydrogen deposits on the Moon. *J. Geophys. Res.* 105 (E2), 4175–4195.

Fisher, A.D., Staelin, D.H., 1977. Possible effect of subsurface inhomogeneities on the lunar microwave spectrum. *Icarus* 32, 98–105.

Gary, B., 1967. Results of a radiometric Moon-mapping investigation at 3 millimeters wavelength. *Astrophys. J.* 147, 245–254.

Gillis, J.J., Joliff, B.L., Elphic, R.C., 2003. A revised algorithm for calculating TiO₂ from Clementine UVVIS data: a synthesis of rock, soil, and remotely sensed TiO₂ concentrations. *J. Geophys. Res.* 108. doi:10.1029/2001JE001515.

Goswami, J.N., Annadurai, M., 2008. Chandrayaan-1 mission to the Moon. *Acta Astronaut.* 63, 1215–1220.

Jin, Y.-Q., Fa, W., 2009. An inversion approach for lunar regolith layer thickness using optical albedo data and microwave emission simulation. *Acta Astronaut.* 65, 1409–1423. doi:10.1016/j.actaastr.2009.03.082.

Keihm, S.J., Langseth, M.G., 1975a. Microwave emission spectrum of the Moon: mean global heat flow and average depth of the regolith. *Science* 187, 64–66.

Keihm, S.J., Langseth, M.G., 1975b. Lunar microwave brightness temperature observations reevaluated in the light of Apollo program findings. *Icarus* 24, 211–230.

Krotikov, V.D., Troitsky, V.S., 1964. Radio emission and nature of the Moon. *Sov. Phys. Usp.* 6, 841–871.

Lawson, S.L., Jakosky, B.M., Park, H.-S., Mellon, M.T., 2000. Brightness temperatures of the lunar surface: calibration and global analysis of the Clementine long-wave infrared camera data. *J. Geophys. Res.* 105 (E2), 4273–4290.

Lucey, P.G., et al., 1996. Lunar titanium content from UV–VIS measurements. *Lunar and Planetary Inst., 27th Lunar and Planetary Science Conference*, pp. 781–782.

Margot, J.L., Campbell, D.B., Jurgens, R.F., Slade, M.A., 2000. Digital elevation models of the Moon from earth-based radar interferometry. *IEEE Trans. Geosci. Remote Sens.* 38, 1122–1133.

Mendell, W.W., Wieczorek, M.A., 1993. Thermogeologic mapping of the moon from lunar orbit. *Lunar and Planetary Inst., 24th Lunar and Planetary Science Conference*, pp. 977–978.

Moffat, P.H., 1972. Aperture synthesis polarimetry of the Moon at 21 cm. *Mon. Not. R. Astron. Soc.* 160, 139–154.

Naugol’naya, M.N., Soboleva, N.S., 2001. A study of the lunar soil in regions with temperature anomalies. *Sol. Sys. Res.* 35, 35–45.

Nozette, S., et al., 1994. The Clementine mission to the Moon: scientific overview. *Science* 266, 1835–1839.

Ono, T., et al., 2009. Lunar radar sounder observations of subsurface layers under the nearside maria of the Moon. *Science* 323, 909–912.

Pettit, E., Nicholson, S.B., 1930. Lunar radiation and temperatures. *Astrophys. J.* 71, 102–135.

Roelof, E.C., 1968. Thermal behavior of rocks on the lunar surface. *Icarus* 8, 138–159.

Schloerb, F.P., Muhleman, D.O., Berge, G.L., 1976. Lunar heat flow and regolith structure inferred from interferometric observations at a wavelength of 49.3 cm. *Icarus* 29, 329–341.

Shorthill, R.W., 1973. Infrared atlas charts of the eclipsed Moon. *Moon* 7, 22–45.

Shorthill, R.W., Saari, J.M., 1965. Nonuniform cooling of the eclipsed Moon: a listing of thirty prominent anomalies. *Science* 150, 210–212.

Wang, Z.Z., Zhang, X.H., Jiang, J.S., Xu, C.D., Zhang, D.H., Guo, W., 2009. Data processing module of Chang’E-1 microwave radiometer and retrieval method of lunar brightness temperature. *Sci. China D* 39, 1029–1044 (in Chinese).

Winter, D.F., 1970. The infrared Moon: data, interpretations, and implications. *Radio Sci.* 5, 229–240.

Zheng, Y.C., Bian, W., Su, Y., Feng, J.Q., Zhang, X.Z., Liu, J.Z., Zou, Y.L., 2009. Brightness temperature distribution of the Moon: result from Chinese Chang’E-1 lunar orbiter. *Geochim. Cosmochim. Acta* 73 (Suppl. 1), A1523 19th V.M. Goldschmidt Conference.

Zisk, S.H., Pettengill, G.H., Catuna, G.W., 1974. High-resolution radar maps of the lunar surface at 3.8-cm wavelength. *Earth Moon Planets* 10, 17–50.